JOURNAL OF SPACECRAFT AND ROCKETS
Vol. 34, No. 6, November–December 1997

# Experimental Investigation of the Flow Structure Near a Single Wraparound Fin

C. P. Tilmann* and R. E. Huffman Jr.†
*U.S. Air Force Wright Laboratory, Wright–Patterson Air Force Base, Ohio 45433*
T. A. Buter‡
*U.S. Air Force Institute of Technology, Wright–Patterson Air Force Base, Ohio 45433*
and
R. D. W. Bowersox§
*University of Alabama, Tuscaloosa, Alabama 35487*

**The flow structure near a single wraparound fin on a wall-mounted semicylindrical model was experimentally investigated at Mach 2.8 ($Re/l = 18 \times 10^6$ m$^{-1}$). Detailed mean flow and turbulence measurements were obtained using conventional pressure probes and cross-wire hot-film anemometry at a series of stations near the fin. Large flowfield asymmetries were observed in both mean flow and turbulence measurements aft of the shock/boundary-layer interaction. Measured turbulence intensities in the fuselage boundary layer were far greater on the concave side of the fin than on the convex side. On the convex side of the fin, the turbulence intensity levels were 30% lower than the preinteraction values, and on the concave side a 50% increase was observed. Similarly, the Reynolds shear stress levels aft of the fin bow shock decreased on the convex side of the fin while increasing dramatically on the concave side. These results are consistent with the stabilizing and destabilizing effects of pressure gradient distortion on supersonic boundary layers.**

## Nomenclature

| | |
|---|---|
| $c$ | = chord length of missile fin, 2.03 cm |
| $K_c$ | = nondimensional turbulent kinetic energy |
| $k$ | = thermal conductivity |
| $l$ | = reference length |
| $l_f$ | = hot-film length |
| $M$ | = Mach number |
| $Nu$ | = Nusselt number |
| $P_{t2}$ | = pitot pressure |
| $Re$ | = reference Reynolds number, $(\rho_\infty u_\infty l)/\mu_\infty$ |
| $Re_e$ | = effective Reynolds number, $(\rho U d/\mu_0)\cos\varphi$ |
| $R_f$ | = hot-film operating resistance |
| $R_{\text{ref}}$ | = hot-film resistance at reference temperature |
| $r$ | = model fin radius of curvature, 1.59 cm |
| $T$ | = temperature, K |
| $T_f$ | = hot-film temperature |
| $u, v, w$ | = mean Cartesian velocity components |
| $x, y, z$ | = Cartesian coordinates |
| $Y$ | = distance from body surface in $y$ direction |
| $\delta_0$ | = reference boundary-layer thickness, 6.1 mm |
| $\theta$ | = horizontal flow angularity, $\tan^{-1}(v/u)$ |
| $\rho$ | = density |
| $\tau_{ij}^T$ | = Reynolds shear stress tensor components, $i \neq j$ |
| $\phi$ | = azimuthal flow angularity, $\tan^{-1}(w/u)$ |
| $\varphi$ | = hot-film incidence angle |
| $()'$ | = Reynolds fluctuating component |
| $(\tilde{})$ | = Favré-averaged component |

Received July 18, 1996; revision received July 1, 1997; accepted for publication July 9, 1997. This paper is declared a work of the U.S. Government and is not subject to copyright protection in the United States.

*Research Engineer, Aeromechanics Division, Flight Dynamics Directorate. Member AIAA.
†Program Test Engineer, Integration Division, Flight Dynamics Directorate. Member AIAA.
‡Assistant Professor, Department of Aeronautics and Astronautics. Senior Member AIAA.
§Assistant Professor, Department of Aerospace Engineering and Mechanics. Senior Member AIAA.

## Introduction

WRAPAROUND fins (WAFs) have been used by designers for several years on low-speed tube-launched missiles and dispenser-launched submunitions. Because stealth capability has become a design parameter for many aircraft, WAFs have become even more attractive for their stowability and reduced cross section. Although WAFs enable many design possibilities, several stability anomalies are inherent for missiles employing them,[1] the most recognized of which is a roll reversal near sonic speeds. Also, due to the asymmetric fin geometry, missiles with WAFs display pitch-yaw coupling. In addition, during recent aeroballistic range tests,[1,2] a possible second rolling moment reversal was observed over a small range of high supersonic speeds ($M \approx 4.5$–$4.7$) on a WAF missile configuration. In this flight regime, yawing moment reversals were also detected.

The majority of experiments performed on WAF missiles have focused on ascertaining stability characteristics via subscale aeroballistic range tests. These experiments provide no detailed flowfield measurements and do little to promote an understanding of the flowfield physics. The current effort experimentally examines the mean and turbulent nature of the flow near a single WAF. Measured flowfield data were obtained at Mach 2.8 on a model composed of a single WAF on a wall-mounted semicylindrical fuselage (Fig. 1). The flow around this test article was surveyed at several stations along its length, concentrating on the region near the fin. Detailed mean flow measurements were obtained using conventional cone-static and pitot pressure probes, as well as hot-film, cross-wire probes. The experiments focused on examining the shock/boundary-layer interaction at the juncture of the fin and the fuselage and on determining its effect on the fuselage boundary-layer characteristics. An understanding of the flowfield near WAFs is critical to further development of such configurations, given the dependence of stability characteristics on Mach number. Determination of the flow structure near a single nonspinning WAF is useful as a first step toward this understanding.

Another objective of this study was to contribute a set of flowfield turbulence data over a three-dimensional fin juncture geometry characterized by a shock/boundary-layer interaction and significant streamline curvature effects. These data augment a building-block dataset,[3] with mean flow and detailed turbulence data, for numerical turbulence model validation, thereby enabling the further numerical

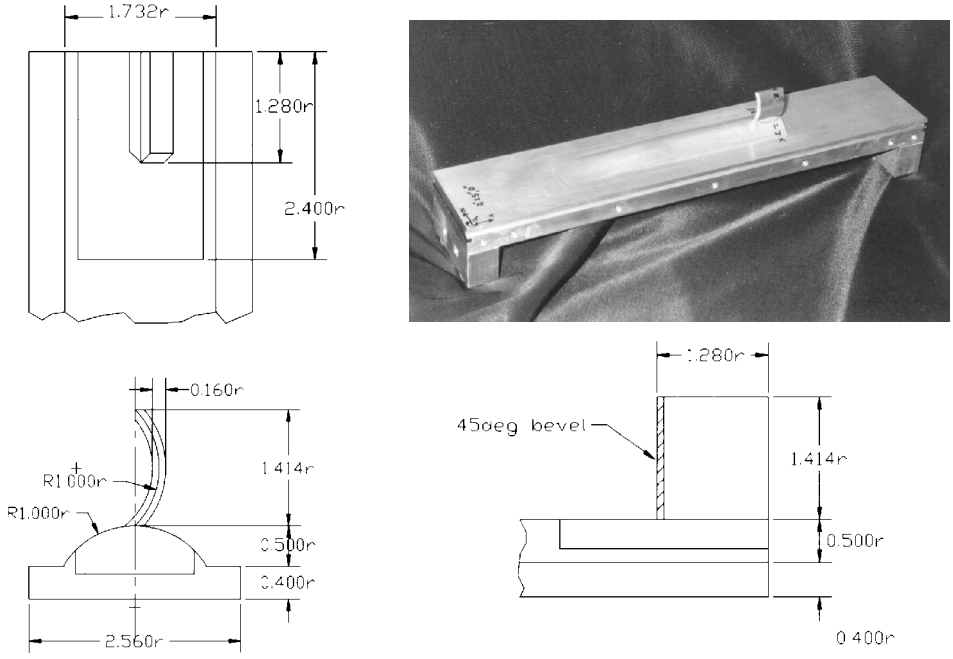


**Fig. 1 WAF model.**

study of WAF configurations over an expanded flight regime. Before this study, no detailed flowfield measurements (mean flow or turbulence) existed for WAF missile configurations. The data gathering criteria of Settles and Dodson[3] were used for guidance.

## Experimental Apparatus

### Test Facility

The experiments took place in an intermittent $M = 2.8$ pressure-vacuum wind tunnel. The settling chamber total pressure and temperature were 2.14 ± 0.02 atm and 294 ± 2 K, respectively, yielding a freestream unit Reynolds number of $Re/l = 18 \times 10^6$ $m^{-1}$. At a location just downstream of the test section entrance (8.4 chord lengths ahead of the fin leading edge), the freestream Mach number was determined to be 2.8 ($U_e = 601$ m/s), with a measurement uncertainty of 2.8%. The boundary layer at this location was fully turbulent with a measured thickness of 5.3 mm at the centerline, defined by the distance from the surface where $M = 0.95\%\ M_e$.

### WAF Model

The investigated WAF model (Fig. 1) was composed of a cylinder of the fin radius $r = 15.9$ mm, blended to a removable test section wall, and had a maximum height of $0.5r$. It was designed to represent a single fin of a typical WAF configuration and was sized to maximize data resolution while avoiding tunnel blockage. The fin had the same proportions as aeroballistic models tested at the Wright Laboratory Armament Directorate,[1,2] with a thickness of $0.2r$, a span of $\sqrt{2}r$, and a chord length of $c = 1.28r$. The leading edge and tip of the fin were beveled at 45 deg (90 deg included angle). The cylinder was $5.12r$ in length, and the single fin was placed at the downstream base. Upstream, the cylinder was blended smoothly to the tunnel wall with a polynomial chosen to ensure second-order continuity in the streamwise direction. The blending region was $5r$ long and started $21.48r$ from the throat of the wind-tunnel nozzle.

### Measurement Apparatus

A Xenon brand 10-ns spark light source was used to create shadowgraph images of the flowfield throughout the test section. A pitot probe and 10 ± 0.03 deg cone-static probe were used to map the pressure topography at various longitudinal stations throughout the test section. These pressure data were used to determine the mean local flow conditions needed for the hot-film data reduction. Two TSI, Inc., brand hot-film probes were used to determine the mass-flux fluctuations of the flow in the tunnel. Both probes were two-component cross-wire hot-film probes, each with two thin films of platinum 1 mm long and 51 $\mu$m in diameter. One probe (TSI model 1243-20) had the films oriented in the vertical ($u$–$v$) plane, angled at ±45 deg to the horizon; the other probe (TSI model 1243AN-20) had its films oriented in the horizontal ($u$–$w$) plane and similarly angled. The transverse separation between the two films was 1 mm. Because the traverse was moving very slowly (about 2.5 mm/s) relative to the flow, pressure and hot-film measurements were taken while the probes were in motion. The hot-film probes were connected to a TSI brand Intelligent Flow Analyzer,[4] which sampled data at 16.6 kHz. An oscilloscope was used to view and to tune the frequency response shape and response time for each film on the probe. Although the probe volume is relatively large, the Reynolds shear stresses measured with these cross wires have been shown to compare very well with laser Doppler velocimetry measurements, obtained in a much smaller probe volume.[5]

## Data Reduction

### Pressure Probes

A pitot probe and a 10-deg (±0.03-deg) cone-static probe were used to measure pressures throughout the flowfield in the test section. Through the manipulation of results from conical and normal shock relations, the pressure data obtained from these probes can be used to calculate the local Mach number. The following curvefit was generated to simplify data reduction[6]:

$$1/M = -0.052976 + 4.6840\xi - 18.6786\xi^2 + 50.7006\xi^3 - 54.1577\xi^4 \quad (1)$$

where $\xi$ is defined as the ratio of the pressure measured with the 10-deg cone-static probe to the pitot pressure. It has been found that for flow angles less than 6.0 deg the errors in Mach number are less than 0.03. Also note that Eq. (1) is valid for Mach numbers in the range from 1.5 to 4.4 and has a standard deviation of 0.06% relative to the exact solution.[6] The usual gasdynamics relations for a calorically perfect gas, with an assumption of constant total temperature, were used to calculate the density and the velocity magnitude.

### Hot-Film Probes

The constant-temperature hot-film anemometer records the voltage required to maintain the film at a constant known temperature. The power required to maintain this temperature is equivalent to the heat transfer $q_f$ between the hot film and the surrounding flow. The Nusselt number can be related to the heat transfer from the film by

$$Nu = \frac{q_f}{\pi k l_f (T_f - T_e)} \quad (2)$$

where $T_e$ is the temperature that the unheated film would approach under these flow conditions (equilibrium temperature). For supersonic flow, where $M_n > 1.2$, the film heat transfer is related to the Reynolds number through the following semiempirical relation[6,7]:

$$Nu = a\sqrt{Re_e} + b \tag{3}$$

The calibration constants $a$ and $b$ are determined by linear least squares regression.

One of the key features of cross-wire anemometry is how the Reynolds turbulent shear stress can be estimated as the negative of the directly measured mass-flux correlation term combined with the density fluctuation. Bowersox and Schetz[6] showed that neglecting third-order terms allows the Reynolds shear stress to be written as

$$\tau_{ij}^T \approx -\bar{\rho}\,\overline{u_i' u_j'} - \overline{u_i}\,\overline{\rho' u_j'} - \overline{u_j}\,\overline{\rho' u_i'} \qquad (i \neq j) \tag{4}$$

$$\tau_{ij}^T \approx -\frac{\overline{(\rho u_i)'(\rho u_i)'}}{\bar{\rho}} + \bar{\rho}\,\overline{u_i}\,\overline{u_j}\,\overline{\left(\frac{\rho'}{\bar{\rho}}\right)^2} \qquad (i \neq j) \tag{5}$$

where the second term is usually much smaller than the first term for small flow angles. This was confirmed for the present experiments by estimating the second term assuming small pressure fluctuations.[8] The second term was always at least an order of magnitude smaller than the first term. Multiple overheat ratios are generally required to determine all of the flow information. However, sensitivity to total temperature fluctuation is often negligible for hot films operating at high overheat ratios, i.e., $R_f/R_{\text{ref}} \geq 2.0$. In cases where the fluctuation in total temperature is negligible, only a single overheat ratio is necessary to determine flowfield information. Because the total temperature fluctuations in the boundary layers were below 2.0% (Ref. 9), a single overheat data reduction method was used.[7]

#### Experimental Uncertainty

To quantify the uncertainty associated with the experiments, the Euclidean ($L_2$) norm is utilized to assess the cumulative effects of error sources. Approximate error bounds on the reduced data were calculated by propagating the measurement errors through the data reduction process, where the equations were linearized. The uncertainty of each experimental result is indicated on all presented data, accounting for probe location, measurement, digitization, and propagation errors associated with the data reduction. Details regarding the uncertainty analysis are contained in Ref. 8.

## Results and Discussion

In the data presentation, the probe position $(x, y, z)$ is nondimensionalized by the fin chord, $c = 20.3$ mm, where the coordinate origin is located at the intersection of the fuselage surface centerline and leading edge of the fin. Negative $x$ values are upstream of the leading edge, and negative $z$ values are to the concave side of the fin. Boundary-layer data are presented as a function of the distance from the model fuselage $Y$. This relative position from the body is normalized by a reference boundary-layer thickness, $\delta_0 = 6.1$ mm, which was measured on the model centerline $0.41c$ ahead of the leading edge of the fin.

The experimental data of the present study are presented with the results of a pilot inviscid numerical simulation[10] that was performed before the experiments were conducted. The inviscid simulation was not intended to be a rigorous computational study but to provide a means of establishing the most suitable locations for the experimental measurements. The calculation was conducted on a grid representing the WAF model as installed in the wind tunnel and assumed inflow boundary conditions based on data that had been previously obtained in an empty test section.[9] In these earlier experiments, the freestream Mach number was determined to be 2.9, and the settling chamber total pressure and temperature were reported to be 2.0 atm and 294 K, respectively.

#### WAF Flowfield Characteristics

To get an initial understanding of the flowfield ahead of the fin, shadowgraph images were obtained with the model in the test section.[10] A shadowgraph image of the region near the fin is presented in Fig. 2. Note how the bow shock remains detached over the full span of the fin at this Mach number. Also, the shock/boundary-layer interaction produces the same type of λ-shock that has been typically observed in front of blunt fins and cylinders mounted on flat plates.[11] Whereas two-dimensional photography indicates flow features similar to those seen on straight fins, conventional pressure probes, hot-film anemometry, and computational fluid dynamics (CFD) all demonstrate that the flow near the fin is highly asymmetric.[8,10,12] This asymmetry can be clearly seen in the computed and measured pitot pressures at the $x = 0.69c$ plane (Fig. 3). On the concave side of the fin, a high-pressure region is produced between the fin and its center of curvature where pitot pressure (and mass-flux levels) are greatly increased over the freestream value. This produces a large region of relatively high surface pressures near the half-span of the fin that contributes to a negative rolling moment. Here, rolling moment will be defined in the vehicle stability sense; thus a negative value indicates a moment acting in the direction of negative curvature. In contrast, the convex side of the

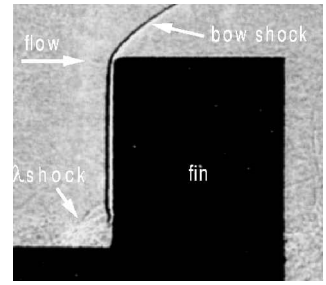


**Fig. 2 Shadowgraph of the fin region.**

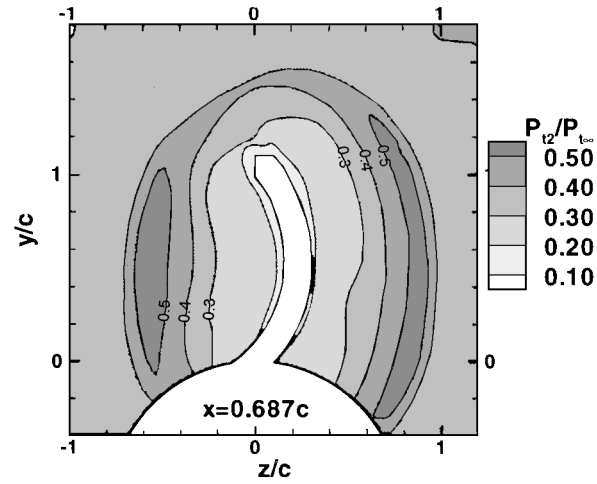


**a) Numerical (Euler)**

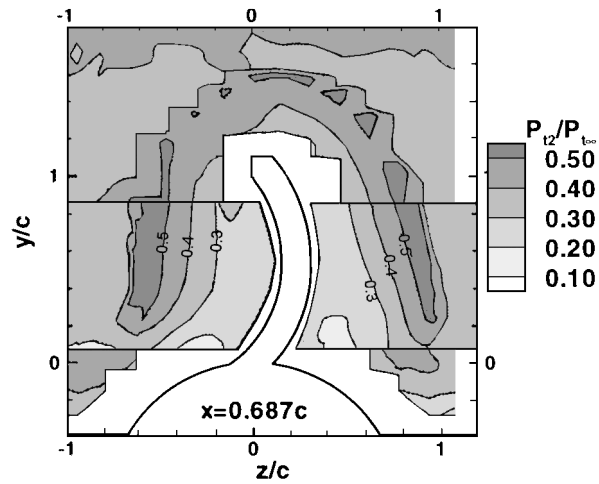


**b) Experimental (±1.2%)**

**Fig. 3 Pitot pressures at $x = 0.69c$.**

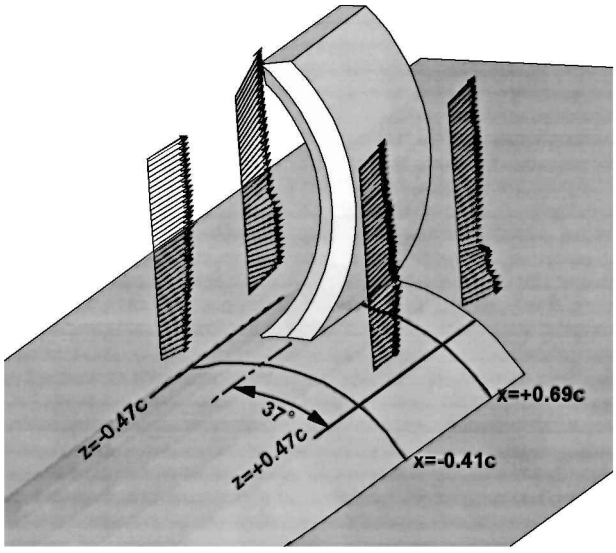


**Fig. 4 Probe locations.**

fin exhibits a structure reminiscent of conical flow, with the pressure gradient in the direction normal to the fin chiefly independent of spanwise location. Agreement between the inviscid numerical results and experiment suggests that the position and strength of the bow shock is, not surprisingly, dominated by inviscid characteristics of the flow except in the immediate vicinity of the fin/body juncture where the fuselage boundary layer becomes important.

**Effect of Shock on Fuselage Boundary Layer**

The fuselage boundary layer was surveyed at four locations on the model as shown in Fig. 4. These locations were chosen to represent the upstream and downstream regions on either side of the fin because two of the stations set the reference for the flow upstream of the fin bow shock (at $x = -0.41c$) and the other two stations were positioned downstream of the shock (at $x = +0.69c$). At each of these axial locations, the flow was surveyed on the concave (Cc) side and on the convex (Cv) side of the fin (at $z = \pm 0.47c$) with pressure probes and hot-film cross wires.

Pressure contours generated by solving the Euler equations[10] are superposed on a side view of the model as a means of illustrating the pressure variation in streamwise planes passing through the measurement stations in Fig. 5. Measurements were obtained at the indicated locations using $u$–$v$ and $u$–$w$ hot-film cross wires, as well as pitot and cone-static pressure probes. Note that the measurement locations are canted slightly to show the effect of the probes flexing as they traverse the tunnel. This effect was included in the data reduction, and the locations at which the numerical solution was surveyed were canted to mimic this flexing.

*Comparison of $u$–$v$ and $u$–$w$ Probes*

The agreement between the axial mean and fluctuating quantities obtained by the two probes was considered excellent (Fig. 6). The small differences were attributed primarily to the flow angles ($\phi \approx \pm 10$ deg) experienced by the probes that have finite (1-mm) film separations. Probe volume effects also induced some uncertainty in regions of the flowfield experiencing large property gradients.

*Mean Flow Measurements*

Mean flow measurements were obtained with a combination of pitot and cone-static pressure probes, as well as hot-film cross wires. The pressures measured directly by the pitot probe are shown in Fig. 7 and show a strong correlation with the mean axial mass-flux provided by the hot-film surveys (Fig. 8). Upstream of the fin, the measurements indicate an undisturbed boundary layer. However, the boundary layer is drastically different on either side of the fin at the downstream survey location. On the convex side, the pitot pressure and mass-flux profiles are characterized by a large inflection within the boundary layer. The flow here has passed through a strong shock resulting in discontinuous pitot pressure and mass-flux

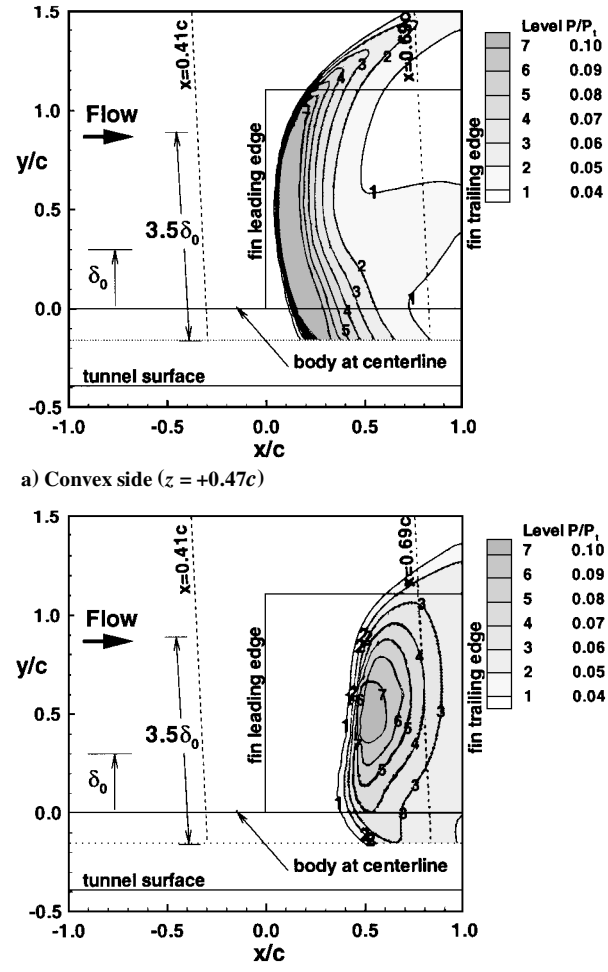


**Fig. 5 Probe location relative to shock given by inviscid computations.**

profiles in the outer boundary layer ($0.3 < Y/\delta_0 < 1.0$). On the concave side, having gone through a somewhat weaker shock, the boundary-layer profile shape has undergone little change. Above $Y/\delta_0 = 0.8$, the fluid at the downstream survey location has experienced an overall compression from its upstream state. Closer to the fuselage ($Y/\delta_0 < 0.5$) there is a small region in which measured pitot pressures do not change. Measured mass-flux values also appear to flatten in this region.

The measured flow angularity (Fig. 9) is also drastically different on the two sides of the fin. Although the measured flow angles outside of the boundary layer agree well with inviscid predictions, viscous effects induce a complicated shock/expansion structure where the shock interacts with the fuselage boundary layer. Here, the shock angles (and structure) are drastically different from those predicted by inviscid methods. These viscous influences induce a large spike in the flow angle $\theta$ on the convex side of the fin (near $Y/\delta_0 \approx 1.1$ in Fig. 9a). This turning effect is not indicated by the inviscid CFD and is believed to be caused by a vortex embedded in the fin/fuselage juncture that entrains fluid and pulls it toward the body. This explanation is consistent with preliminary viscous numerical results,[8] the complete findings of which will be the subject of a future article. On the concave side of the fin, although the measured $\theta$ profile is similar to that predicted with inviscid CFD, there are differences in magnitude.

The azimuthal component of the flow angularity is presented in Fig. 9b. At the downstream survey location ($x = 0.69c$) on the concave side, the outer flow ($Y/\delta_0 > 1.5$) is strongly directed away from the fin, at flow angles $\phi$ up to 10 deg at the midspan ($Y/\delta_0 \approx 2.5$). However, over a small region inside the boundary layer ($0.5 < Y/\delta_0 < 1.0$), the flow is angled with similar levels toward the fin. This effect is likely to be a combination of the flow wrapping around the fin and an expansion that reflects off of the bow shock as a

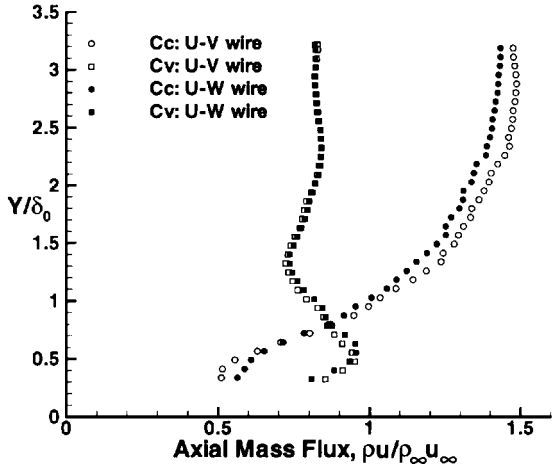


a) Axial mass-flux, $\rho u'/\rho u_\infty$

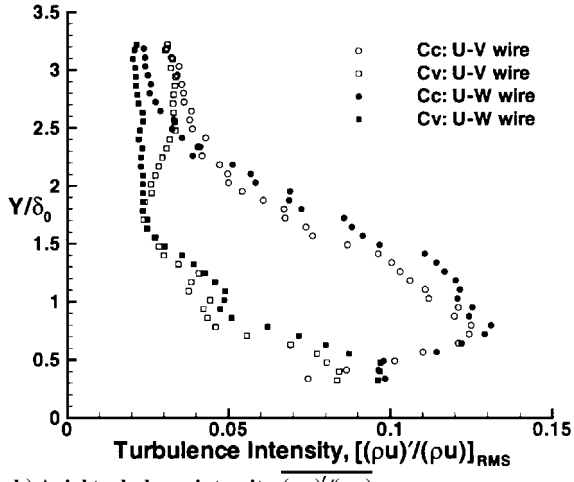


b) Axial turbulence intensity, $\overline{(\rho u)'/(\rho u)}$

**Fig. 6 Comparison of cross-wire probe orientation at $x = 0.69c$ ($\pm 11\%$).**

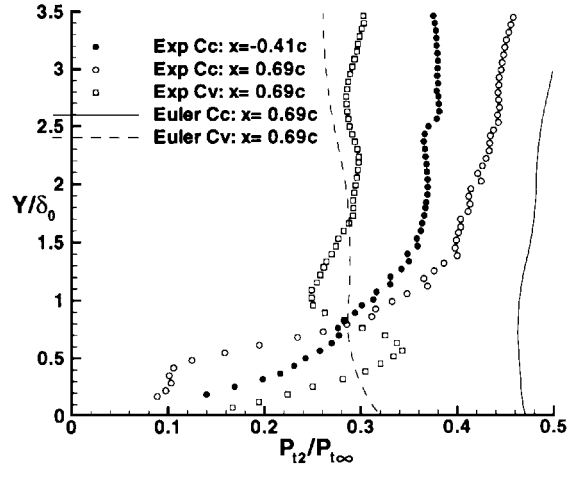


**Fig. 7 Pitot pressure ($\pm 1.2\%$).**

compression. Conversely, on the convex side, the flow is nearly parallel to the fin's surface, agreeing well with inviscid results. The wave structure, which is also seen in the pitot data, is observed in the $0.5 < Y/\delta_0 < 1.0$ region in both flow angles due to the juncture vortex.

An understanding of the flowfield near WAFs is critical to further development of WAF missile configurations, given the dependence of stability characteristics on Mach number. These experimental mean flow data provide a benchmark for future computational simulations that may provide a more detailed description of the flowfield.

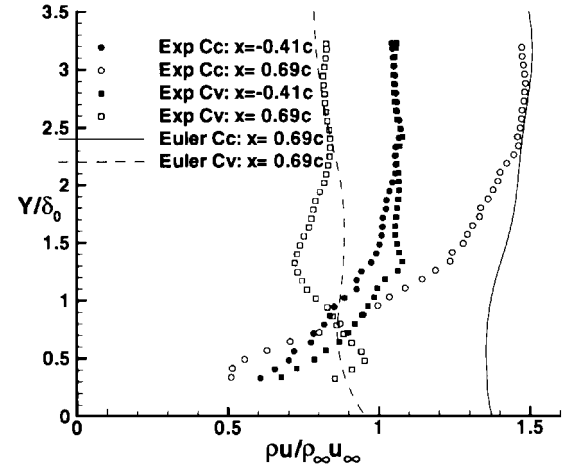


**Fig. 8 Axial mass flux $\rho u/\rho u_\infty$ (cross film, $\pm 11\%$).**

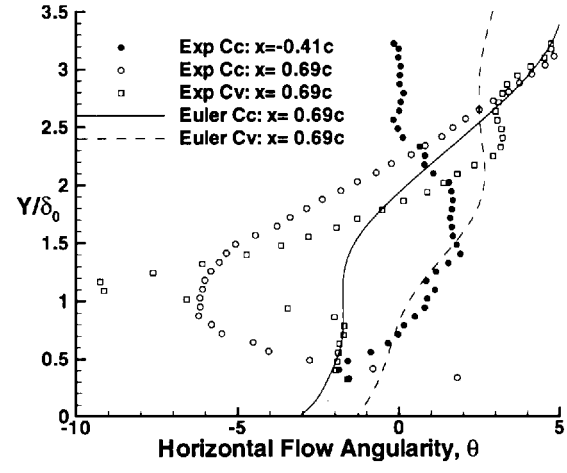


a) Horizontal flow angularity, $\theta$ (deg)

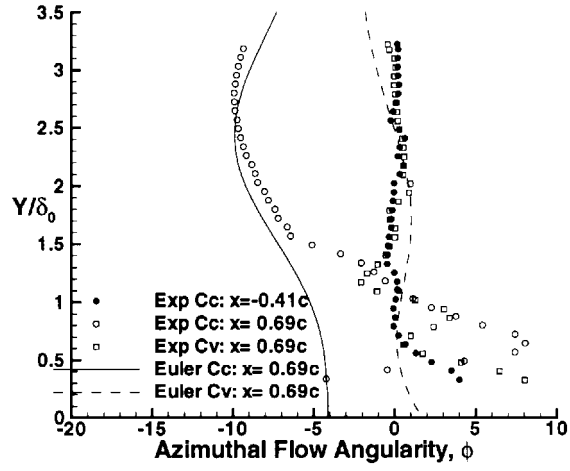


b) Azimuthal flow angularity, $\phi$ (deg)

**Fig. 9 Flow angularity ($\pm 15.0\%$).**

*Turbulence Measurements*

Although the downstream probe location on the concave side of the fin is in a region of mild favorable pressure gradient, it is still close to the bow shock. Examination of the turbulence intensity in this region indicates that the shock induces an increase in the axial and transverse turbulence intensity (Fig. 10), which is consistent with the destabilizing effects of adverse pressure gradients on turbulent boundary layers.[13]

On the convex side, the turbulence intensities at the same streamwise location are far lower because the flow has experienced a favorable pressure gradient over an extended streamwise distance (Fig. 5). Expansions have been reported to stabilize or reduce the turbulence levels in boundary layers.[13] Also contributing to this dramatic

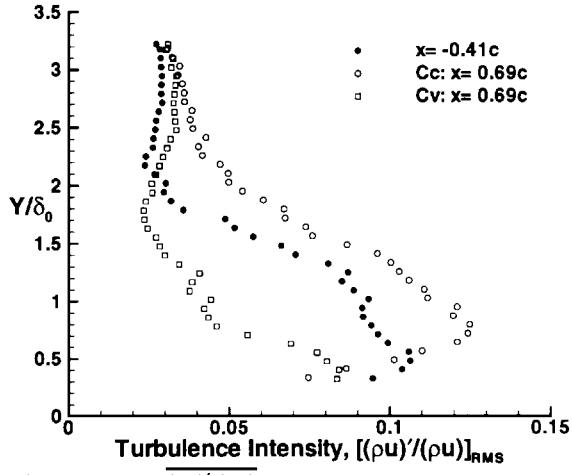


a) $x$ component, $\overline{(\rho u)'/(\rho u)}$

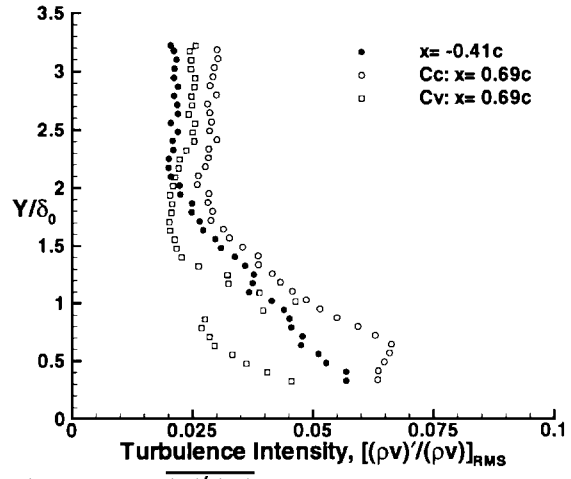


b) $y$ component, $\overline{(\rho v)'/(\rho u)}$

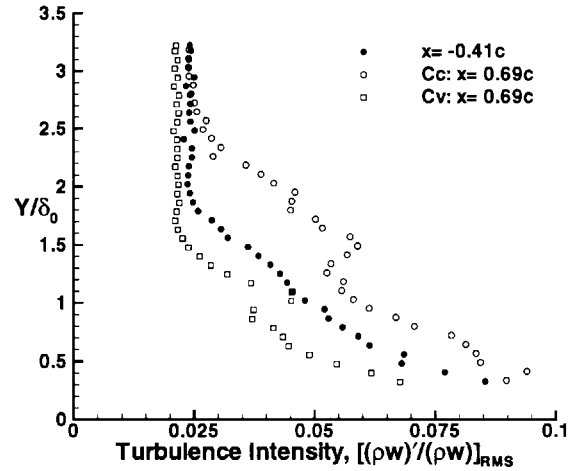


c) $z$ component, $\overline{(\rho w)'/(\rho u)}$

**Fig. 10 Turbulence intensity profiles (±11%).**

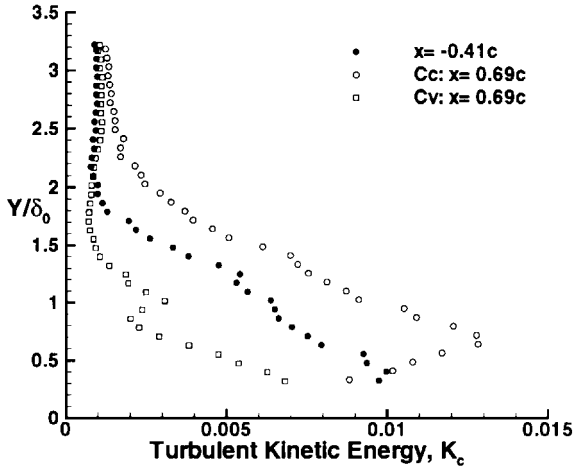


**Fig. 11 TKE, $K_c$ [Eq. (6), ±16%].**

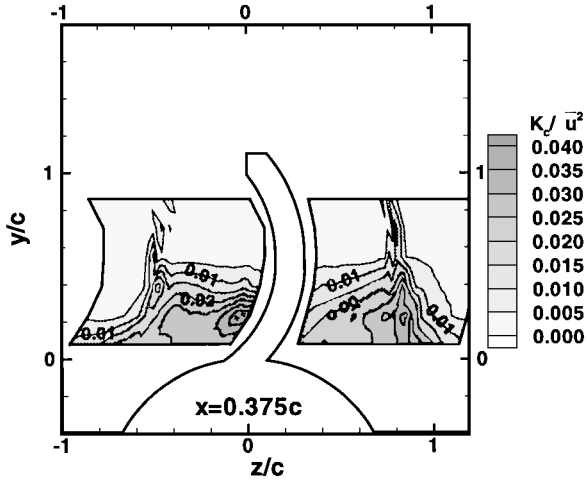


a) $x = 0.37c$

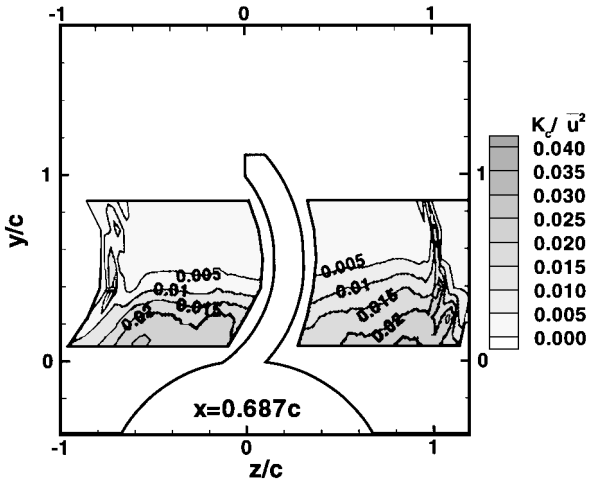


b) $x = 0.69c$

**Fig. 12 TKE, $K_c$ [Eq. (6), ±16%].**

recovery is the rapid flow acceleration induced by the convex curvature of the fin. Both of the secondary mass-flux turbulence intensities experience a sharp rise near $Y/\delta_0 = 1.1$, where similar discontinuities are observed in the mean flow angularity (notably $\theta$).

The net effects of the bow shock and fin curvature are illustrated in Figs. 11 and 12 via the nondimensional turbulent kinetic energy (TKE) $K_c$ defined by

$$K_c = \frac{1}{2}\left\{\overline{\left[\frac{(\rho u)'}{\overline{\rho u}}\right]^2} + \overline{\left[\frac{(\rho v)'}{\overline{\rho u}}\right]^2} + \overline{\left[\frac{(\rho w)'}{\overline{\rho u}}\right]^2}\right\} \qquad (6)$$

The TKE is significantly elevated on the concave side of the fin and reduced on the convex side relative to values upstream of the shock (Fig. 11).

The nondimensional TKE at two streamwise stations is shown in Fig. 12: one at the same location as the boundary-layer measurements ($x = +0.69c$) and one farther upstream at $x = +0.38c$. These surveys, which included the upper portion of the boundary layer, indicate that TKE levels on the convex side are markedly greater than those on the concave side at both stations. Also, TKE is dissipating in the axial direction on both sides of the fin, as the flow passes through regions of favorable pressure gradient. Thus, as the

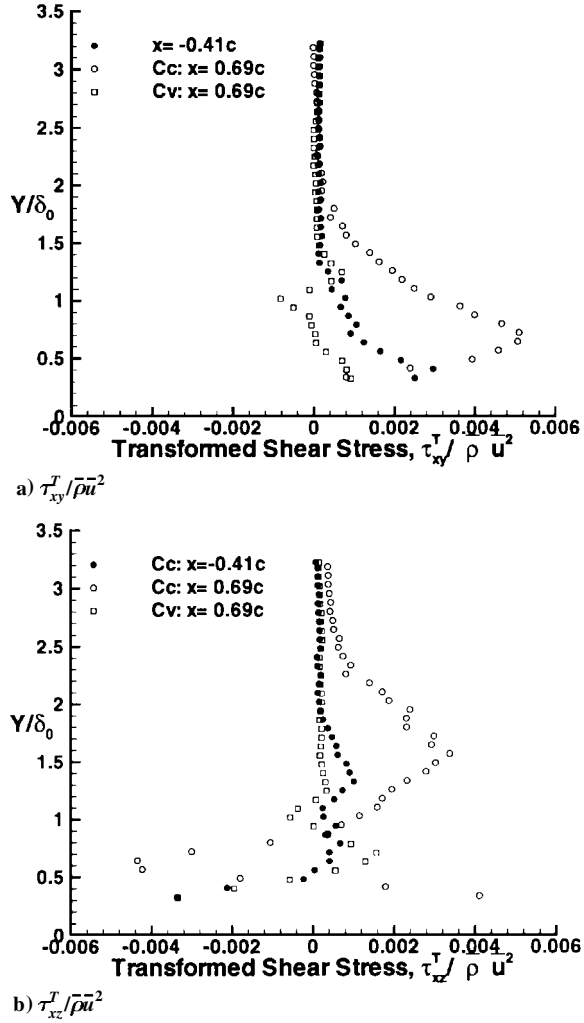


**Fig. 13 Measured turbulent shear stresses [Eq. (5), ±21%].**

flow continues to recover, the TKE levels on the concave side of the fin are likely to continue decreasing in the downstream direction, possibly to the levels seen on the convex side.

The boundary-layer stabilizing and destabilizing effects on either side of the fin are also apparent in the Reynolds shear stresses measured with the cross wire (Fig. 13). Upstream of the fin, the shear stress profile corresponds to that of an undisturbed boundary layer, with levels comparable to those upstream of the model. This indicates that the effects of the compression caused by the blended region of the model have been damped to levels comparable to an equilibrium turbulent boundary layer. Note that the second term of the total turbulent shear stress in Eq. (5) has been determined to be at least an order of magnitude smaller than the first term for all surveyed regions. Therefore, only the total turbulent shear stress is presented.

On the convex side of the fin, a reduction of turbulent shear stress with downstream position is indicative of the strong stabilizing effect of favorable pressure gradient. Indeed, as observed by other researchers investigating correlations between streamline distortion and turbulence,[14] the expansion associated with a favorable pressure gradient can result in reduced (or even negative) turbulent shear stress. Conversely, the turbulent shear stress on the concave side is increased by roughly 100–200%, commensurate with the previously noted increases in turbulence intensity and TKE. This pattern is consistent with other measurements obtained in regions of large compression.[14] Note, too, that the boundary-layer thickness has dramatically increased (by about 60–70%) on the concave side, whereas it was reduced slightly on the convex side.

Before this study, no detailed mean flow or turbulence measurements existed for WAF missile configurations. The present experiments have produced a significant amount of turbulence data on this shock/boundary-layer interaction flowfield. It is expected that these turbulence data will be useful for validation of turbulence closure models intended to predict flows having large pressure gradients.

## Conclusions

The mean and turbulent structure of the flowfield near a single WAF mounted on a semicylindrical body has been characterized experimentally at a Mach number of 2.8. In this experiment, the flow around the model was surveyed at several stations along its length, concentrating on the region near the fin. Although the boundary layer on the fin was determined to be too thin to survey with pressure or hot-film cross-wire probes, the boundary layer on the missile fuselage was easily explored using these devices. The result was a mapping of the pressure, velocity, and turbulent properties near the fin. From these measurements, several significant conclusions were drawn.

The structure of the mean flow near the WAF can be divided into four distinct regions downstream of the fin bow shock. Two of the regions are outside of the fuselage boundary layer—one region on each side of the fin. After passing through the bow shock, the outer flow on the convex side of the fin passes through a region of large favorable pressure gradient. On the concave side of the fin, however, this expansion is partially offset by the compressive effect of the fin curvature. These outer regions have been modeled using inviscid numerical methods with excellent results. The remaining two regions are within the fuselage boundary layer. On the convex side of the fin, the fin attachment angle produces a high-pressure region near the fin/fuselage juncture in the inviscid numerical results. Experimental surveys on this side of the fin indicate large inflections in pressure and flow angularity through the boundary layer. On the concave side, the experiments indicate an expansion effect and what is believed to be flow separation near the fuselage.

This study has shown that both inviscid and viscous processes play roles in determining the structure of the flowfield near WAFs. The outer flowfield exhibits asymmetries brought about by the effects of pressure gradient, streamline curvature, and differing shock/expansion structures, whereas viscous phenomena apparently induce irregularities in the flowfield near the fuselage that may be important to the overall aerodynamic loading. That said, many aspects of the flowfield were accurately captured by solving the Euler equations. The bow shock created by the WAF is an inviscid phenomenon. Except in the immediate vicinity of the fin/body intersection where the bow shock interacts with the missile body boundary layer, the pressure field is dominated by inviscid effects. This has been demonstrated through the excellent agreement between measured quantities and those predicted by inviscid numerical methods in the outer region of the flow. The shock remains detached over the full span of the fin at this Mach number, and its interaction with the fuselage boundary layer creates the same type of λ-shock associated with blunt fins in supersonic flowfields.

The reduction of data from the pitot, cone-static, and hot-film cross-wire probes produced a significant amount of turbulence data. Before this study, no detailed mean flow or turbulence measurements existed for WAF missile configurations. These data yielded some interesting insights. As expected, the bow shock causes a dramatic increase in TKE and Reynolds shear stress on both sides of the fin. The flow experiences an expansion as it passes the fin, which reduces the turbulence intensity. However, for a fixed streamwise location, the reduction is far greater on the convex side of the fin, where the flow experiences a stronger favorable pressure gradient over a longer distance. This results in lower turbulence intensities and lower, though still significant, shear stresses. These findings are consistent with previous research on the effects of favorable and adverse pressure gradients on supersonic turbulent boundary layers.

## Acknowledgment

It is with great appreciation that the authors thank Gregg Abate from the Armament Directorate of U.S. Air Force Wright Laboratory for sponsoring this work.

## References

[1] Abate, G. L., "Aerodynamic Research of Wrap Around Fin Missile Configurations and Alternative Wrap Around Fin Designs," Armament Directorate, Wright Lab., WL-TR-94-7015, Eglin AFB, FL, Feb. 1994.

[2]Vitale, L. R. E., Abate, G. L., Winchenbach, G. L., and Riner, W., "Aerodynamic Test and Analysis of a Missile Configuration with Curved Fins," AIAA Paper 92-4495, Aug. 1992.

[3]Settles, G. S., and Dodson, L. J., "Supersonic and Hypersonic Shock/Boundary-Layer Interaction Database," *AIAA Journal*, Vol. 32, No. 7, 1994, pp. 1377–1383.

[4]*IFA 100 System: Instruction Manual*, TSI, Inc., St. Paul, MN, 1987.

[5]Bowersox, R. D. W., "Combined Laser Doppler Velocimetry and Cross-Wire Anemometry Analysis for Supersonic Turbulent Flow," *AIAA Journal*, Vol. 34, No. 11, 1996, pp. 2269–2275.

[6]Bowersox, R. D. W., and Schetz, J. A., "Compressible Turbulence Measurements in a High-Speed High Reynolds Number Mixing Layer," *AIAA Journal*, Vol. 32, No. 4, 1994, pp. 758–764.

[7]Bowersox, R. D. W., "Thermal Anemometry," *Handbook of Fluid Dynamics and Fluid Machinery*, edited by J. Schetz and W. Fuhs, Wiley, New York, 1996, pp. 965–983.

[8]Tilmann, C. P., "Numerical and Experimental Investigation of the Flowfield Near a Wrap-Around Fin," Ph.D. Thesis, School of Engineering, Air Force Inst. of Technology, Wright–Patterson AFB, OH, March 1997.

[9]Miller, R., Dotter, J., Bowersox, R. D. W., and Buter, T. A., "Compressible Turbulence Measurements in Supersonic Boundary Layers with Favorable and Adverse Pressure Gradients," *Journal of Fluids Engineering*, FED-Vol. 224, 1995, pp. 193–200.

[10]Tilmann, C. P., Huffman, R., Buter, T. A., and Bowersox, R. D. W., "Characterization of the Flow Structure in the Vicinity of a Wrap-Around Fin at Supersonic Speeds," AIAA Paper 96-0190, Jan. 1996.

[11]Dolling, D. S., and Bogdonoff, S. M., "Blunt Fin-Induced Shock Wave Turbulent Boundary Layer Interaction," *AIAA Journal*, Vol. 20, No. 12, 1982, pp. 1674–1680.

[12]Huffman, R., Tilmann, C. P., Buter, T. A., and Bowersox, R. D. W., "Experimental Flow Structure Investigation of a Wrap-Around Fin at Mach 2.9," AIAA Paper 96-2450, June 1996.

[13]Spina, E., Smits, J., and Robinson, K., "The Physics of Supersonic Turbulent Boundary Layers," *Annual Review of Fluid Mechanics*, Vol. 26, Jan. 1994, pp. 287–319.

[14]Bowersox, R. D. W., and Buter, T. A., "Mass-Weighted Turbulence Measurements in a Mach 2.9 Boundary Layer Including Mild Pressure Gradients," *AIAA Journal*, Vol. 34, No. 12, 1996, pp. 2479–2483.

J. C. Adams Jr.
*Associate Editor*